Pseudo Landau level representation of twisted bilayer graphene: Band topology and implications on the correlated insulating phase

Jianpeng Liu, Junwei Liu, and Xi Dai
Department of Physics, Hong Kong University of Science and Technology, Kowloon, Hong Kong

We propose that the electronic structure of twisted bilayer graphene (TBG) can be understood as Dirac fermions coupled with opposite pseudomagnetic fields generated by the moiré pattern. The two low-energy flat bands from each monolayer valley originate from the two zeroth pseudo Landau levels of Dirac fermions under such opposite effective magnetic fields, which have opposite sublattice polarizations and carry opposite Chern numbers ± 1, giving rise to helical edge states in the gaps below and above the low-energy bulk bands near the first magic angle. We argue that small Coulomb interactions would split the eightfold degeneracy (including valley and physical spin) of these zeroth pseudo Landau levels, and may lead to insulating phases with nonvanishing Chern numbers at integer fillings. Besides, we show that all the high-energy bands below or above the flat bands are also topologically nontrivial in the sense that for each valley the sum of their Berry phases is quantized as $\pm\pi$. Such quantized Berry phases give rise to nearly flat edge states, which are dependent on truncations on the moiré length scale. Our paper provides a complete and clear picture for the electronic structure and topological properties of TBG, and has significant implications on the nature of the correlated insulating phase observed in experiments.

Twisted bilayer graphene (TBG) is an engineered system with one graphene layer stacked on top of the other and rotated by a twisted angle θ, which exhibits various interesting properties [1–7]. Around the so-called "magic angles," the low-energy electronic structures of TBG are characterized by four nearly flat bands contributed by the two monolayer valleys [2], and these flat low-energy bands are believed to be responsible for the correlated insulating phases [8–12] and unusual superconductivity [12–14]. Numerous theoretical attempts have been made to understand the electronic structures [15–25], the structural properties [26–28], the correlated insulating phase [15,29–38], and the mechanism of superconductivity [15,30,32,33,35,39–44]. However, up to now, the nature of the correlated insulating phase and the superconductivity are still obscure. The system thus becomes a platform to study the unconventional physics driven by Coulomb correlations.

Besides many-body effects, the four low-energy bands already exhibit interesting or even puzzling properties at the single-particle level [15–20]. In particular, recently it has been shown that the four low-energy bands are topologically nontrivial in the sense that they are characterized by odd windings of Wilson loops. However, despite the numerical evidence [19] and the mathematical classifications [19,45], how to physically understand and describe the topological nature of the flat bands in TBG is still an open question. On the other hand, so far the topological properties of the high-energy bands have rarely been discussed. To fully understand the unusual electronic and topological properties of TBG, a clear and complete physical picture is needed.

We address these issues in this paper and reach the following conclusions. We find that in the small twist angle limit, the low-energy electronic structures of TBG can be viewed as 2D Dirac models under pseudomagnetic fields generated by the moiré pattern. The nontrivial topology of the two low-energy bands for each valley originates from the two zeroth pseudo Landau levels (LLs) of Dirac fermions with such opposite effective magnetic fields. The two zeroth LLs (for each valley) carry opposite Chern numbers ± 1 and possess opposite sublattice polarizations. They are decoupled from each other as a result of an emergent chiral symmetry in the low-energy subspace. This leads to two pairs of helical edge states in the energy gaps below and above the low-energy bands of TBG. As the four low-energy bands (of the two valleys) in TBG are equivalent to four zeroth pseudo LLs (per spin), small Coulomb interactions are expected to split the pseudo LL degeneracy at integer fillings, and could lead to insulating states with fully polarized zeroth pseudo LLs and nonvanishing total Chern numbers, as possibly suggested by the recent experiments on 3/4-filled [9] and $\pm 1/4$-filled TBG [12] around the first magic angle. In particular at $\pm 3/4$ filling, only one out of the eight zeroth pseudo LLs (including physical spin) is occupied (empty), which would give rise to a ferromagnetic state with nonvanishing Chern number ± 1.

In addition to the low-energy bands, we show that for each valley the high-energy bands below and above the low-energy bands are also topologically nontrivial with quantized Berry phases $\pm\pi$. Such quantized Berry phases give rise to two nearly flat edge states in the gaps between the high-energy bands and the low-energy bands, which are dependent on the truncations on the moiré length scale. Last, we find that the topological gaps between the high-energy bands and the low-energy bands can be significantly enhanced by atomic corrugations, and that changing the corrugation strength may further drive transitions between insulating and semimetallic phases.

The paper is organized as follows. In Sec. I, we discuss the lattice structure of TBG and introduce the continuum model describing the electronic structures of TBG. In Sec. II, we introduce the pseudo-LL representation of TBG, which provides a clear physical picture for the topological properties of the low-energy bands, and has significant implications on the nature of the correlated insulating phases observed in experiments. In Sec. III, we discuss the topological properties of the high-energy bands and the truncation dependence of the edge states. In Sec. IV, we discuss in detail the effects of atomic corrugations on the electronic structures of TBG. In Sec. V, we make a summary.

I. THE TBG SYSTEM AND THE CONTINUUM MODEL

As shown in Fig. 1(a), the commensurate moiré pattern is formed when the top-layer graphene is rotated with respect to the bottom layer by certain angles $\{\theta(m)\}$, where m is an integer obeying the condition $\cos\theta(m) = (3m^2 + 3m + 1/2)/(3m^2 + 3m + 1)$ [46]. The lattice vectors of the moiré superlattice are expressed as $\mathbf{t}_1 = (\sqrt{3}L_s/2, L_s/2)$, and $\mathbf{t}_2 = (0, L_s)$, where $L_s = |\mathbf{t}_1| = a/[2\sin(\theta/2)])$ is the size of the moiré supercell, with $a = 2.46$ Å being the lattice constant of monolayer graphene. The K (K') points of the two monolayers K_1 (K'_2) and K_2 (K'_1) are respectively mapped to K_s and K'_s points in the moiré supercell Brillouin zone (BZ) as shown in Fig. 1(b).
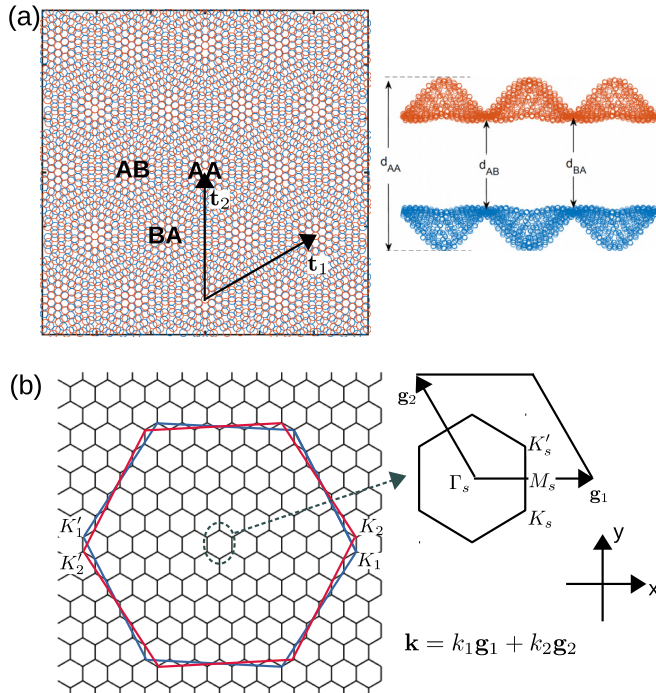
FIG. 1. (a) Left: A top view of the moiré pattern of twisted bilayer graphene for $m = 5$ ($\theta \approx 6.01°$). The solid and dashed lines represent lattice truncations through the AA regions and the AB/BA regions, respectively. The two arrows denote the lattice vectors. Right: Illustration of atomic corrugations. (b) The Brillouin zones of the top monolayer, bottom monolayer, and the moireé supercell are plotted in red, blue, and black lines, respectively.

Locally homogeneous regions are formed in the moiré pattern of TBG. In some regions, the $A(B)$ sublattice of the top layer is mostly on top of the same sublattice of the bottom layer, and such regions are dubbed as the AA region as shown in Fig. 1(a); while, in some other regions, the $B(A)$ sublattice of the top layer is on top of the $A(B)$ sublattice of the bottom layer, which are marked as $AB(BA)$ regions. It is worth noting that the interlayer distance in TBG varies in real space [47]. In the $AB(BA)$ region, the interlayer distance $d_{AB} \approx 3.35$ Å while in the AA-stacked region the interlayer distance $d_{AA} \approx 3.6$ Å [48]. Such atomic corrugations may be modeled as [17]

$$d_z(\mathbf{r}) = d_0 + 2d_1 \sum_{j=1}^{3} \cos[\mathbf{b}_j \cdot \delta(\mathbf{r})], \quad (1)$$

where $\mathbf{b}_1 = [2\pi/a, 2\pi/(\sqrt{3}a)]$, $\mathbf{b}_2 = [-2\pi/a, 2\pi/(\sqrt{3}a)]$, and $\mathbf{b}_3 = \mathbf{b}_1 + \mathbf{b}_2$ are three reciprocal lattice vectors of monolayer graphene. $\delta(\mathbf{r})$ is a 2D vector indicating the local in-plane shift between the carbon atoms in the two layers around position $\mathbf{r}$ in the moiré supercell. In the AA region $\delta \approx (0, 0)$ while in the AB region $\delta \approx (0, a/\sqrt{3})$. We take $d_0 = 3.433$ Å and $d_1 = 0.0278$ Å to reproduce the interlayer distances in AA- and AB-stacked bilayer graphene.

The electronic structure of TBG can be described by the Bloch states around the Dirac points in the two graphene monolayers which mutually tunnel to each other, and can be formulated by a continuum model proposed by Bistritzer and MacDonald [2]. Using such a continuum model of TBG, Bistritzer and MacDonald found that for each monlayer valley (K or K') there are two low-energy bands, the bandwidths of which vanish recurrently at a series of "magic angles" starting from $\sim 1.05°$ [2]. The states from the two monolayer valleys K and K' are assumed to be decoupled from each other, because the scattering amplitudes are negligibly small at small twist angles [2,46].

To be specific, the continuum model describing the TBG system for the K valley is expressed as

$$H^+(\hat{\mathbf{k}}) = \begin{pmatrix} -\hbar v_F(\hat{\mathbf{k}} - \mathbf{K}_1) \cdot \sigma & U e^{-i\Delta\mathbf{K}\cdot\mathbf{r}} \\ U^\dagger e^{i\Delta\mathbf{K}\cdot\mathbf{r}} & -\hbar v_F(\hat{\mathbf{k}} - \mathbf{K}_2) \cdot \sigma \end{pmatrix}, \quad (2)$$

where v_F is the bare Fermi velocity of the Dirac cone in gaphene, $\hat{\mathbf{k}} = -i\partial_\mathbf{r}$, and $\mathbf{K}_1$ and $\mathbf{K}_2$ are the $\mathbf{K}$ points of the bottom and top layers as shown in Fig. 1(b). The Pauli matrices $\sigma = (-\sigma_x, \sigma_y)$ are defined in the space of the A, B sublattices of graphene. The tunneling between the Dirac states in the two layers is described by the 2×2 matrix U

$$U = \begin{pmatrix} u_0 g(\mathbf{r}) & u'_0 g(\mathbf{r} - \mathbf{r}_{AB}) \\ u'_0 g(\mathbf{r} + \mathbf{r}_{AB}) & u_0 g(\mathbf{r}) \end{pmatrix}, \quad (3)$$

where $\mathbf{r}_{AB} = (\sqrt{3}L_s/3, 0)$, u'_0 and u_0 denote the intersublattice and intrasublattice interlayer tunneling amplitudes, $u_0 < u'_0$ if the effects of atomic corrugations are taken into account [17]. $\Delta\mathbf{K} = \mathbf{K}_2 - \mathbf{K}_1 = (0, 4\pi/3L_s)$ is the shift between the Dirac points of the two monolayers, and the phase factor $g(\mathbf{r})$ is defined as $g(\mathbf{r}) = \sum_{j=1}^{3} e^{i\mathbf{q}_j \cdot \mathbf{r}}$, with $\mathbf{q}_1 = (0, 4\pi/3L_s)$, $\mathbf{q}_2 = (-2\pi/\sqrt{3}L_s, -2\pi/3L_s)$, and $\mathbf{q}_3 = (2\pi/\sqrt{3}L_s, -2\pi/3L_s)$.

The continuum model of each valley has the symmetry generators C_{3z}, $C_{2z}\mathcal{T}$, and C_{2x}, where $\mathcal{T}$ is the time-reversal operation for spinless fermions (i.e., complex conjugation). The two valleys can be mapped to each other by $\mathcal{T}$, C_{2z}, or C_{2y} operations. Moreover, there is an additional particle-hole-like symmetry which transforms $H^+(\hat{\mathbf{k}})$ to the Hamiltonian of the other valley $H^-(\hat{\mathbf{k}})$:

$$\Lambda H^+(\hat{\mathbf{k}})\Lambda^{-1} = -H^-(\hat{\mathbf{k}}), \tag{4}$$

where $\Lambda = i\tau_y\sigma_x$.

II. THE PSEUDO-LANDAU-LEVEL REPRESENTATION OF TWISTED BILAYER GRAPHENE

A. The pseudo-Landau-level representation and the band topology

In this section, we show that the two low-energy bands (per valley) in TBG can be represented by the two zeroth pseudo LLs carrying opposite Chern numbers. We will focus on the K valley, i.e., the Hamiltonian in Eq. (2). The Hamiltonian of the other valley can be obtained by a time-reversal operation.

First we note that the constant wave vectors $\mathbf{K}_1$ and $\mathbf{K}_2$ in Eq. (2) can be gauged by applying the following transformations to the basis Bloch functions,

$$\psi_{ls}(\mathbf{r}) \rightarrow \psi_{ls}(\mathbf{r})e^{i\mathbf{K}_l \cdot \mathbf{r}}, \tag{5}$$

where $l = 1, 2$ and $s = A, B$ refer to the layer and sublattice degrees of freedom, respectively. Then Eq. (2) becomes

$$H^+(\mathbf{k}) = \begin{pmatrix} -\hbar v_F\mathbf{k}\cdot\sigma & U \\ U^\dagger & -\hbar v_F\mathbf{k}\cdot\sigma \end{pmatrix}. \tag{6}$$

Next we expand the phase factors $g(\mathbf{r})$ and $\mathbf{g}(\mathbf{r} \pm \mathbf{r}_{AB})$ in Eq. (3) to the linear order of r/L_s, and rewrite Eq. (6) in the following form:

$$H^+(\mathbf{k}) = -\hbar v_F\left(\mathbf{k} - \frac{e}{\hbar}\mathbf{A}\tau_y\right)\cdot\sigma + 3u_0\tau_x, \tag{7}$$

where the Pauli matrices τ and σ are defined in the space of the two layers and the two sublattices, respectively, with $\sigma = (-\sigma_x, \sigma_y)$. The effective vector potential is $\mathbf{A} = (2\pi u_0')/(L_s e v_F)(y, -x)$. In the end, we transform to the basis that diagonalizes τ_y, i.e.,

$$\psi_{\alpha,s}(\mathbf{r}) = \frac{1}{\sqrt{2}}[\psi_{1,s}(\mathbf{r}) + i\psi_{2,s}(\mathbf{r})],$$

$$\psi_{\beta,s}(\mathbf{r}) = \frac{1}{\sqrt{2}}[\psi_{1,s}(\mathbf{r}) - i\psi_{2,s}(\mathbf{r})], \tag{8}$$

where $\psi_{ls}(\mathbf{r})$ with layer index $l = 1, 2$ and sublattice index $s = A, B$ is the Bloch function of the monolayer graphene at $\mathbf{K}_l$ from the s sublattice. In this basis, Eq. (2) eventually becomes

$$H^+(\hat{\mathbf{k}}) = \begin{pmatrix} -\hbar v_F(\hat{\mathbf{k}} - \frac{e}{\hbar}\mathbf{A})\cdot\sigma & -3iu_0 \\ 3iu_0 & -\hbar v_F(\hat{\mathbf{k}} + \frac{e}{\hbar}\mathbf{A})\cdot\sigma \end{pmatrix}. \tag{9}$$

Again, the gauge field $\mathbf{A} = (2\pi u_0')/(L_s e v_F)(y, -x)$. Without the off-diagonal term $\pm 3iu_0$, Eq. (9) is nothing but two Dirac fermions coupled to opposite effective magnetic fields $\pm\mathbf{B}_s = \pm\nabla\times\mathbf{A}$ with the magnitude $B_s = 3u_0'\Delta K/(ev_F)$, where $\Delta K =$

$4\pi/(3L_s)$ is the distance between the two Dirac points in the two layers. It is known that $u_0' \approx 0.1$ eV [2,17] and $\hbar v_F \approx 5.25$ eVÅ, then we estimate $B_s \approx 120$ T for $\theta \approx 1.08°$.

Let us first neglect the off-diagonal term $\pm 3iu_0$, then Eq. (9) becomes exactly solvable. The eigenenergies are just the LLs of the Dirac fermions, $E_{\pm Nk} = \pm\hbar\omega_c\sqrt{N}$, with $N \geqslant 0$ being an integer. The corresponding cyclotron frequency ω_c and the magnetic length l_B are

$$\hbar\omega_c = \sqrt{\frac{8\pi\hbar v_F u_0'}{L_s}}, \quad l_B = \sqrt{\frac{L_s\hbar v_F}{4\pi u_0'}}. \tag{10}$$

Equation (9) can be readily obtained [49]. The eigenfunctions of the upper (α) and lower (β) diagonal blocks of Eq. (9) (in the Landau gauge) are expressed as

$$\phi_{\pm Nk}^\alpha(x, y) = \frac{1}{\sqrt{2L_x l_B}}e^{ikx}\begin{pmatrix} \mp\Psi_N(\xi) \\ \Psi_{N-1}(\xi) \end{pmatrix},$$

$$\phi_{\pm Nk}^\beta(x, y) = \frac{1}{\sqrt{2L_x l_B}}e^{-ikx}\begin{pmatrix} \Psi_{N-1}(\xi) \\ \pm\Psi_N(\xi) \end{pmatrix}, \tag{11}$$

where $\xi = y/l_B - l_B k$, and $\Psi_N(\xi) = 1/(2^{N/2}\sqrt{N!}\pi^{1/4})e^{-\xi^2/2}H_N(\xi)$ is the eigenfunction of the 1D quantum harmonic oscillator, with $H_N(\xi)$ being the Hermite polynominal with $N \geqslant 0$. The wavevector $k = 2\pi j/L_x$ is the index for the LL degeneracy with the integer $0 \leqslant j \leqslant L_x L_y/(2\pi l_B^2)$, and L_x and L_y denote the size of the system along the x and y directions. These eigenstates have the interesting property that the zeroth LLs in the upper and lower diagonal blocks have exactly opposite sublattice polarizations. The two zeroth pseudo LLs also carry opposite Chern numbers ± 1 [49], which is the origin of the odd winding pattern of the Wilson loops [see blue lines in Fig. 4(b)].

Now we consider the off-diagonal term $\pm 3iu_0$ in Eq. (9) (denoted as H_T^+ hereafter) that couples the pseudo LLs in the upper and lower diagonal blocks. First, we note that the coupling term H_T^+ is *intrasublattice* but, as discussed above, the two zeroth pseudo LLs have exactly opposite sublattice polarizations. Therefore, the direct coupling within the subspace of zeroth pseudo LLs exactly vanishes. To be specific, in the pseudo-LL basis H_T^+ (after transforming to the Landau gauge) can be rewritten as

$$\langle\phi_{\lambda'N'k'}^\alpha|H_T^+|\phi_{\lambda Nk}^\beta\rangle = \frac{-3iu_0 l_B}{2L_x}[-\lambda'\Psi_{N'}(l_B k)\Psi_{N-1}(l_B k') \\ + \lambda\Psi_{N'-1}(l_B k)\Psi_N(l_B k')], \tag{12}$$

where $\lambda, \lambda' = \pm$ denote the upper and lower branches of the LLs, and $N \geqslant 0$. Equation (12) clearly indicates that the direct coupling between the two zeroth pseudo LL vanishes, and that the coupling is stronger for higher pseudo LLs with larger N indices. This means that the higher pseudo LLs would be strongly coupled with each other and would lose their topological character. The zeroth pseudo LL from the upper (lower) diagonal block could be coupled with the higher LLs from the lower (upper) diagonal block, which would give rise to a finite bandwidth (denoted by W) to the otherwise exactly flat zeroth pseudo LLs. However, a straightforward calculation using perturbation theory indicates the

TABLE I. Pseudo LL spacings ($\hbar\omega_c$) and the low-energy bandwidths (W) at different twist angles (in units of eV).

m	15	20	25	30	31	32	33
$\hbar\omega_c$	0.441	0.384	0.344	0.315	0.310	0.305	0.300
W	0.274	0.125	0.041	0.007	0.014	0.020	0.025

leading-order energy correction to the zeroth pseudo LL is on the order of $u_0^3/(\hbar\omega_c)^2$. Therefore, the topological character of the zeroth pseudo LLs is expected to be unchanged as long as the pseudo LL spacing $\hbar\omega_c$ is greater than the bandwidth induced by u_0. In Table I, we show the pseudo LL spacings $\hbar\omega_c$ and the bandwidths W of the low-energy bands at different twist angles in TBG, which is calculated using the continuum model shown in Eq. (2). Clearly $\hbar\omega_c$ becomes much greater than the low-energy bandwidth W when $m \gtrsim 15$ ($\theta \lesssim 2.03°$).

B. The edge states of the pseudo Landau levels

Neglecting the off-diagonal term $\pm 3iu_0$, the two zeroth pseudo LLs of opposite Chern numbers would give rise to a pair of helical gapless edge states. However, the two zeroth pseudo LLs could be coupled indirectly by tunneling to the higher LLs with the amplitude $\sim u_0^3/(\hbar\omega_c)^2$. Thus, such high-order couplings will open a gap in the edge states $\sim u_0^3/(\hbar\omega_c)^2 \approx 5$ meV at $\theta \approx 1.08°$. On the other hand, the pseudo-LL picture discussed above is valid for the leading-order expansion of (r/L_s). At a nonvanishing twist angle θ, the $\mathcal{O}(r/L_s)^2$ term would also (weakly) couple the two zeroth pseudo LLs, which would open a gap in the otherwise gapless edge states. Therefore, one expects to see two pairs of slightly gapped helical edge states in the energy gaps below and/or above the bulk low-energy bands, which are contributed by the two monolayer valleys.

A microscopic Slater-Koster tight-binding model based on the carbon p_z orbitals [50,51] is adopted to calculate the edge states of TBG. To be specific, the hopping integral between two p_z orbitals at different carbon sites i and j (in either of the two layers) is expressed in the Slater-Koster form,

$$t(\mathbf{d}) = V_\sigma \left(\frac{\mathbf{d} \cdot \hat{\mathbf{z}}}{d} \right)^2 + V_\pi \left[1 - \left(\frac{\mathbf{d} \cdot \hat{\mathbf{z}}}{d} \right)^2 \right], \quad (13)$$

where $V_\sigma = V_\sigma^0 e^{-(r-d_c)/\delta_0}$ and $V_\pi = V_\pi^0 e^{-(r-a_0)/\delta_0}$. $\mathbf{d} = (d_x, d_y, d_z)$ is the displacement vector between the two carbon sites. $a_0 = a/\sqrt{3} = 1.42$ Å, $d_c = 3.35$ Å is the interlayer distance in AB-stacked bilayer graphene, and $\delta_0 = 0.184\,a$. $V_\sigma^0 = 0.4$ eV and $V_\pi^0 = -2.7$ eV. The atomic corrugations are modeled by Eq. (1), and their effects can be taken into account in the tight-binding model by plugging Eq. (1) into Eq. (13).

We have constructed a ribbon of TBG at the first magic angle using the above Slater-Koster tight-binding model. The ribbon has translation symmetry along the y direction, and has a finite width ~ 68 nm (six moiré cells) along the x direction. The red and black lines in Fig. 2 denote the states localized at the two edges, while the blue lines represent the bulk bands. Clearly, at each edge there are two pairs of slightly gapped helical edge states in the two bulk energy gaps below and above the low-energy bands. The gaps in the edge states are
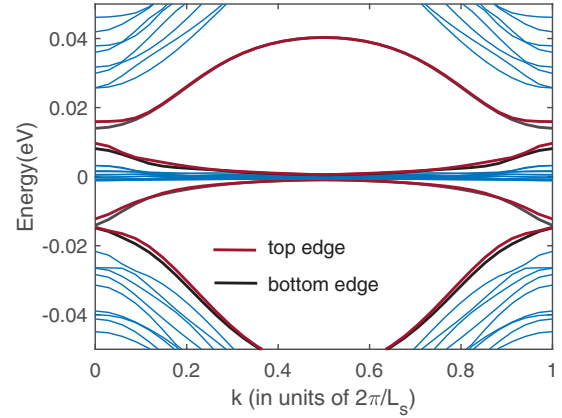
FIG. 2. The band structure of twisted bilayer graphene at $\theta \approx 1.08°$ in a ribbon geometry with the open boundary condition. The red and black lines represent the edge states from the two edges of the ribbon and blue lines represent the bulk states.

due to the couplings between the LLs in the two blocks, and the magnitudes of the gaps ~ 3–10 meV, in agreement with the previous argument. As a comparison, the bulk band structure at $\theta \approx 1.08°$ calculated using the same tight-binding model is shown in Fig. 4(a) in blue lines.

C. Robustness of the Wilson loops at finite twist angles

1. Symmetry analysis of the Wilson-loop operators

At finite twist angles, the $\mathcal{O}(r/L_s)^2$ terms become nonnegligible, which would directly couple the two zeroth pseudo LLs. However, numerically the Wilson loops of the flat bands in TBG retain the their topological character even at large twist angles [49]. It turns out that the odd winding pattern of the Wilson loops [see the blue circles in Fig. 4(b)] is protected by $C_{2z}\mathcal{T}$ [19,45] and C_{2x} symmetries [19].

To be explicit, denoting the Wilson loop of the two flat bands at k_2 (integrated along k_1) by a 2×2 matrix $\hat{w}(k_2)$, we find that they obey the following relationship due to the constraints from the $C_{2z}\mathcal{T}$ and C_{2x} symmetries:

$$\begin{aligned} w_{mn}(k_2) &= -\xi_m \xi_n w_{mn}^*(k_2) - j_n \delta_{mn}, \\ w_{mn}(k_2) &= w_{mn}(-k_2) - j_n' \delta_{mn}, \end{aligned} \quad (14)$$

where $w_{mn}(k_2)$ is the matrix element of $\hat{w}(k_2)$, j_n and j_n' are arbitrary integers, and m, n are the band indices. ξ_m, $\xi_n = \pm 1$ are the eigenvalues of the $C_{2z}\mathcal{T}$ operator for the energy bands m and n. The first line of Eqs. (14) is from the $C_{2z}\mathcal{T}$ symmetry, which indicates that the diagonal element of the Wilson loop operator $w_{nn}(k_2) = j_n$. Moreover, for $\xi_m \xi_n = \pm 1$, the off-diagonal element $w_{mn}(k_2) = \mp w_{mn}^*(k_2)$ for $m \neq n$. Therefore, for a two-band system there is only one parameter describing the variation of $\hat{w}(k_2)$ with respect to k_2,

$$\hat{w}(k_2) = \begin{pmatrix} j_1 & 0 \\ 0 & j_2 \end{pmatrix} + \begin{cases} d_y(k_2)\sigma_y, & \text{if } \xi_1\xi_2 = 1 \\ d_x(k_2)\sigma_x, & \text{if } \xi_1\xi_2 = -1, \end{cases} \quad (15)$$

where j_1 and j_2 are two arbitrary integers and σ_x and σ_y are the Pauli matrices in the space of the two bands. Equation (15) guarantees that a band touching point in the Wilson-loop spectrum is topologically stable, which cannot be gapped out
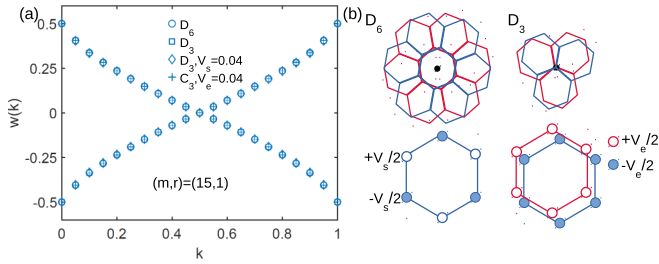
FIG. 3. (a) The Wilson loops of the four low-energy bands of twisted bilayer graphene at $m = 15$ ($\theta \approx 2.13°$). The blue circles, squares, diamonds, and plus signs represent the microscopic configurations with D_6 symmetry, D_3 symmetry, D_3 symmetry with staggered sublattice potential $V_s = 0.04$ eV, and D_3 symmetry with vertical electric field $V_e = 0.04$ eV, respectively. (b) A schematic illustration of the different microscopic configurations.

unless two touching points meet each other and get annihilated. This is consistent with the conclusion in Refs. [19,45]. Moreover, Eq. (15) also suggests that the sum of the Wilson-loop eigenvalues of the two flat bands can only take integer values. The second line of Eqs. (14) is from the C_{2x} symmetry, which dictates that the Wilson loop at k_2 equals to that at $-k_2$ [19] with some integer ambiguity in the trace. Such a constraint requires that the degeneracy points in the Wilson loop have to either occur in pairs at k_2 and $-k_2$ or at the high-symmetry points $k_2 = 0$ and/or 0.5 (in reduced coordinates). This is why the Wilson-loop spectra retain their topological character even at finite twist angles.

2. Robustness of the Wilson loops against microscopic perturbations

The microscopic symmetry group of TBG depends on the stacking pattern and the choice of the rotation center. For example, if before the rotation the top layer is exactly stacked on top of the bottom layer, and one takes the center of the hexagon as the rotation center, then the resulted moiré superlattice has the highest symmetry D_6 as considered by Song *et al.* [19]. If the rotation center is chosen at one of the carbon atoms, then the resulting moiré structure has a D_3 symmetry, which is the case considered in most of the previous literature. If the rotation center is chosen at an arbitrary point, then the only symmetry the system has is C_{2y} where the "y" axis is along one of the morie lattice vectors. On the other hand, the two flat bands from each valley at small twist angles have been shown to be equivalent to two zeroth LLs with opposite Chern numbers. The pseudomagnetic fields would lead to a new magnetic length scale l_B given by Eqs. (10). Clearly l_B is much greater than the microscopic lattice constant for small twist angles, thus one expects that the topological properties of the zeroth pseudo LLs should be robust regardless of the perturbations on the microscopic scale.

Using the microscopic tight-binding model introduced in Eq. (13), we would like to explicitly demonstrate that the topological character of the Wilson loops of the four low-energy bands remains robust regardless of the microscopic details. In particular, we have considered different microscopic symmetries in the tight-binding model as schematically shown in Fig. 3(b): (i) the D_6 symmetry where the two layers are

first stacked exactly on top of each other. then rotated about the center of the hexagon; (ii) the D_3 symmetry where the rotation center is at one of the carbon atoms instead of at the hexagon center; (iii) based on the D_3 configuration, we apply a staggered potential $V_s = 0.04$ eV on A and B sublattices in both layers; (iv) still based on the D_3 configuration, we apply a vertical electric field with energy $V_e = 0.04$ eV, which breaks the D_3 symmetry to C_3 symmetry. The Wilson loops of the four low-energy bands at $m = 15$ with these four different microscopic configurations are presented in Fig. 3(a), and are represented by blue circles, squares, diamonds, and plus signs, respectively. Clearly, the Wilson loops with different microscopic symmetries almost exactly overlap with each other, indicating that the topological character of the four low-energy bands is robust against perturbations on the microscopic scale.

D. The implications on the correlated insulating phases

The pseudo-LL representation of TBG has significant implications on the correlated insulating phases observed in experiments [8–12]. We have shown that the flat bands around the magic angles in TBG are equivalent to four zeroth LLs of Dirac fermions contributed by the two valleys K and K'. The direct couplings between the two zeroth LLs (in each valley) vanish due to an emergent chiral symmetry in the zeroth LL subspace. These four zeroth LLs carry different Chern numbers (C) and sublattice polarizations (s). In particular, from the monolayer K valley the two zeroth LLs are $\{C = +1, s = A\}$, and $\{C = -1, s = B\}$; while for the K' valley, the two zeroth LLs have $\{C = +1, s = B\}$, $\{C = -1, s = A\}$. Since the kinetic energy is completely quenched in the LL, any Coulomb interactions are expected to split the eight-fold (including physical spin) degenerate zeroth pseudo LLs, which would possibly lead to insulating phases at any filling factor that could completely fill up an integer number of LLs, namely at 0, $\pm 1/4$, $\pm 1/2$, and $\pm 3/4$ fillings of the low-energy flat bands (including valley and spin), as has been observed in a recent experiment [12]. Since each pseudo LL carries nonvanishing Chern number ± 1, it is then quite natural that many of these phases could have nonzero total Chern number as suggested by the recent experiments on the possible quantum anomalous Hall effect in TBG [9,12]. In particular, at $\pm 3/4$ filling, only one out of the eight pseudo LLs is occupied (empty), which would be split from the other LLs due to exchange interactions. Such a polarized pseudo-LL state has to be ferromagnetic and carries Chern number ± 1, which naturally explains the experimental observations of anomalous Hall effect, ferromagnetism, and the hints of chiral edge states at 3/4 filling of TBG [9].

In realistic situations, the Coulomb interaction is dependent on the layer and sublattice degrees of freedom in graphene. Transforming to the zeroth pseudo LL basis [Eq. (11)], it means that the interaction would become dependent on the Chern number (C) and sublattice (s) polarizations of the zeroth pseudo LLs. The $\{C, s\}$ dependence of the Coulomb interaction would break the degeneracy of the insulating states at the integer fillings. The unambiguous determination of the correlated insulating ground states at the different fillings requires a microscopic and self-consistent
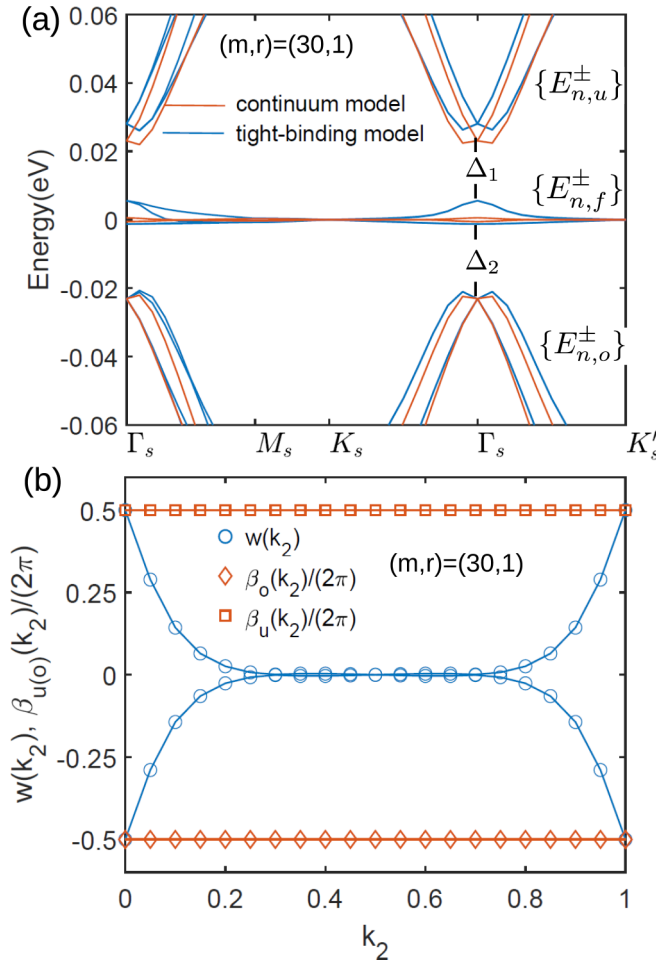
FIG. 4. (a) Bulk band structure of TBG at $(m, r) = (30, 1)$ calculated from the microscopic tight-binding model (blue) and the continuum model (red), including effects of atomic corrugations. (b) The total Berry phases of all the bands below (above) the four flat bands at $(m, r) = (30, 1)$ are denoted by $\beta_o(k_2)$ [$\beta_u(k_2)$], and the Wilson loops of the four flat bands at $(m, r) = (30, 1)$ denoted by $w(k_2)$.

FIG. 5. Edge states in twist bilayer graphene at $m = 15$: (a), (b) the edge states below the four low-energy bands and (c), (d) above the four low-energy bands. (a), (c) The system truncated through the *AA* region; (b), (d), the system truncated through the *BA* and *AB* regions. The inset shows the bulk band structure for $(m, r) = (15, 1)$, where energy windows for the edge states are marked in light blue shadow.

calculation, which is beyond the scope of the present paper and we will leave it for future study.

III. TOPOLOGY OF THE HIGH-ENERGY BANDS

A. Berry phases of the high-energy bands

We continue to discuss the topological properties of the high-energy bands. We first introduce the bulk band structures before demonstrating the topology of the high-energy bands. The bulk band structures at $m = 30$ ($\theta \approx 1.08°$), including effects of atomic corrugations are shown in Fig. 4(a). The blue and red lines indicate the band structures calculated using the microscopic tight-binding model [Eq. (13)] and the continuum model [Eq. (2)], respectively. The calculated gaps at Γ_s above and below the four flat bands [denoted as Δ_1 and Δ_2 in Fig. 2(a)] are around 25 meV, which are in qualitative agreement with the experimental data [8] and the theoretical calculations with fully relaxed structures [26,52].

Such large band gaps actually originate from the atomic corrugations: the *intersublattice* interlayer tunneling u'_0 generates opposite effective magnetic fields which tend to create the topological gaps, while the *intrasublattice* interlayer tunneling u_0 tend to couple the zeroth pseudo LL in one diagonal block to the higher pseudo LLs of the other diagonal block, which reduces the topological gaps. Therefore, the gaps between the low-energy bands and high-energy bands would increase due to the atomic corrugations, because the ratio u_0/u'_0 decreases as a result of the atomic corrugations [17]. This also implies that the topological properties and electronic structures of TBG can be significantly engineered using atomic corrugations, which we will discuss in detail in Sec. IV.

For clarity's sake, we divide all the energy bands in TBG into three groups: all the bands below and above the four low-energy bands are denoted by $\{E_{n,o}^{\pm}\}$ and $\{E_{n,u}^{\pm}\}$, respectively, and the four low-energy bands are denoted by $\{E_{n,f}^{\pm}\}$, where the superscripts $+$ and $-$ are indices for the two monolayer valleys K and K'. In addition to the four low-energy bands, we find that the high-energy bands $\{E_{n,o}^{\pm}\}$ and $\{E_{n,u}^{\pm}\}$ are also topologically nontrivial. To be specific, if the Berry phase integrated along the k_1 direction for the nth band in the group of $\{E_{n,o(u)}^{\pm}\}$ is denoted by $\beta_{n,o(u)}^{\pm}(k_2)$, then

$$\beta_o^{\pm}(k_2) \equiv \sum_n \beta_{n,o}^{\pm}(k_2) = \mp\pi,$$

$$\beta_u^{\pm}(k_2) \equiv \sum_n \beta_{n,u}^{\pm}(k_2) = \pm\pi. \quad (16)$$

The quantization of the total Berry phases shown in Eqs. (16) is guaranteed by the $C_{2z}\mathcal{T}$ symmetry of the continuum model. Equations (16) has been numerically verified by implementing the continuum model of TBG in the plane-wave basis [49], and are plotted in Fig. 4(b) for $m = 30$ ($\theta = 1.08°$), where

the red diamonds and squares represent $\beta_o^+(k_2)$ and $\beta_u^+(k_2)$, respectively. For completeness, in Fig. 4(b) we also plot the Wilson loops of the two flat bands (for one valley) as marked by the blue circles. Thus, Fig. 4(b) presents the complete band topology of TBG.

B. Truncation dependence of the edge states

The nontrivial Berry phase of the high-energy bands implies that for each valley there would be an edge state extending through the 1D edge Brillouin zone. Moreover, because the $+$ and $-$ valleys are mapped to each other by the particle-hole-like operation as shown in Eq. (4), the two edge states contributed by the two valleys may occur in the gaps below and above the four low-energy bands, respectively. In Figs. 5(a) and 5(c), we plot the spectral functions at the edge of TBG at $m=15$ ($\theta \approx 2.13°$) in the band gaps below and above the four low-energy bands. Clearly, there are two nearly flat edge states in the gaps above and below the four low-energy bands contributed by the two valleys. The edge states shown in Figs. 5(a) and 5(c) are calculated when the system is truncated through the AA region. If, instead, the system is truncated through the BA and AB region, then the two nearly flat edge states in the charge gaps disappear, as shown in Figs. 5(b) and 5(d). The truncation dependence of the edge states is reminiscent of the property of the 1D SSH chain with quantized Berry phase $\pm\pi$ [53,54]. The difference is that the truncation dependence of the edge states of the TBG system occurs on the moiré length scale (instead of of the microscopic lattice scale), and the edge states are present when the system is truncated through the AA region regardless of the orientation of the edge. For comparison, we also plot the corresponding bulk band structure in the inset of Fig. 5, where the shaded regions mark the energy windows for the edge-state calculations. It is worth noting that the edge states at $\theta \approx 1.08°$ shown in Fig. 2 would smoothly evolve to those shown in Figs. 5(a) and 5(c) ($\theta \approx 2.13°$) if one of the two helical edge states gets merged into the bulk bands, leaving the other one in the bulk gap. This indicates the consistency between the high-energy and low-energy band topology.

IV. CORRUGATION-ENHANCED TOPOLOGICAL GAPS AND TOPOLOGICAL TRANSITIONS

In this section, we study in detail how atomic corrugations affect the electronic structures and topological properties of TBG. We have numerically checked that once the atomic corrugations are taken into account, the four low-energy bands are separated from the other bands by nonvanishing direct gaps from $m=5$ all the way to $m=33$ [49]. It implies that the system remains topologically nontrivial for all these twist angles. The edge states predicted above thus may be a strong evidence of the nontrivial band topology in TBG.

We further explore how the topological gaps are dependent on the corrugation strength parameterized by d_1 [see Eq. (1)] and the twist angle $\theta(m)$. In Fig. 6(a), we plot the the indirect gap between $\{E_{n,f}^\pm\}$ and $\{E_{n,u}^\pm\}$ in the parameter space spanned by d_1 and the integer m. The horizontal axis is d_1 ranging from -0.05 Å to 0.05 Å, and the vertical axis is m, where $m=5$ corresponds to $\theta \approx 6.01°$ and $m=33$ corresponds to $\theta \approx 1.02°$.
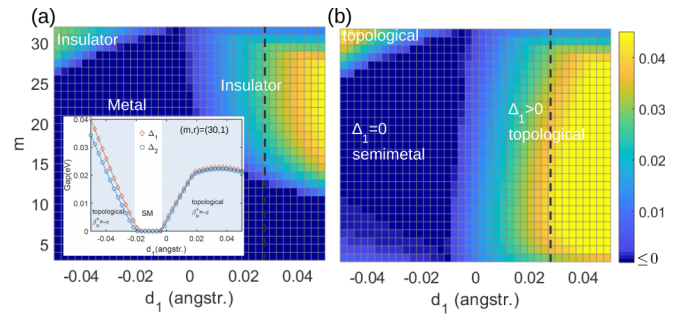
FIG. 6. (a) Color map of the indirect gap above the four flat bands in TBG, in units of eV. The horizontal axis is the corrugation strength parameterized by d_1 [see Eq. (1)], and the vertical axis is the integer m characterizing the rotation angle. (b) Color map of the direct gap above the four flat bands at Γ_s. The dashed black lines in (a) and (b) mark the actual atomic corrugation strength.

When $m \lesssim 11$ ($\theta \gtrsim 2.88°$), the system is always metallic for -0.05 Å $\leqslant d_1 \leqslant 0.05$ Å. When $m \geqslant 12$, a global gap opens up as d_1 increases from -0.05 Å, indicating a transition from a metallic to a topologically nontrivial insulating phase. When $m \approx 30$ ($\theta \approx 1.08°$), the system is mostly insulating and only becomes (semi)metallic in a small window of d_1.

In Fig. 6(b), we plot the direct gap above the four low-energy bands at Γ_s as denoted by Δ_1 in Fig. 4(a). We see that when $m \lesssim 26$, Δ_1 is almost exactly zero for -0.05 Å $\lesssim d_1 \lesssim 0$; when $m \gtrsim 26$ Δ_1 gradually diminishes as d_1 decreases from 0.05 Å, vanishes at some critical value d_{1c}, then reopens at another critical value d_{1c}^*. It is interesting to note that the topological character of both the four low-energy bands and the high-energy bands are *unchanged* after such band-touching events at Γ_s. This is because there is (approximate) particle-hole symmetry in the low energy spectrum at Γ_s, such that the band touchings almost occur simultaneously for Δ_1 and Δ_2, but the band topology is not expected to be changed after an even number of band-touching events. This is clearly shown in the inset of Fig. 6(a), where we plot Δ_1 (red diamonds) and Δ_2 (blue circles) as a function of d_1 for $m=30$.

V. SUMMARY

To summarize, in this paper we have proved that the two flat bands (per valley) near the magic angles in TBG originate from the two zeroth LLs of Dirac fermions threaded by opposite effective magnetic fields generated by the moiré pattern. The direct coupling between the two zeroth LLs is forbidden by an emergent chiral symmetry in the low-energy subspace. As a consequence, the two flat bands possess opposite Chern numbers ± 1 and exhibit the odd winding pattern in the Wilson loops. This gives rise to two pairs of helical edge states in the bulk gaps between the low-energy and the high-energy bands at the first magic angle. The pseudo LL representation of the flat bands in TBG have significant implications on the correlated insulating phase observed in experiments. We have argued that Coulomb interactions may split the eightfold degenerate (including physical spin) zeroth pseudo LLs, and possibly lead to insulating states with polarized pseudo LLs with nonvanishing Chern numbers when an integer number

of the pseudo LLs are filled up, as suggested by the recent experiments [9,12]. In particular, at $\pm 3/4$ fillings, the insulating ground states may be spin- polarized states with nonvanishing Chern numbers ± 1, which is consistent with the recent experimental observations at 3/4 filling [9].

We have further shown that the high-energy bands of TBG are topologically nontrivial, which are characterized by constant and quantized Berry phases $\pm \pi$ and protected by $C_{2z}\mathcal{T}$ symmetry. The quantized Berry phases give rise to a pair of nearly flat edge states in the energy gaps below and above the four low-energy bands. These edge states are robust regardless of the orientation of the edge but are dependent on the truncations on the moiré length scale. We also find that the topologically nontrivial gaps between the flat bands and the high-energy bands are significantly enhanced due to atomic corrugations. Our work is a step forward in understanding the electronic properties of TBG, and have significant implications on the correlated insulating phase and superconductivity observed in TBG.

ACKNOWLEDGMENTS

[1] J. M. B. Lopes dos Santos, N. M. R. Peres, and A. H. Castro Neto, Phys. Rev. Lett. **99**, 256802 (2007).

[2] R. Bistritzer and A. H. MacDonald, Proc. Natl. Acad. Sci. USA **108**, 12233 (2011).

[3] G. Li, A. Luican, J. L. Dos Santos, A. C. Neto, A. Reina, J. Kong, and E. Andrei, Nat. Phys. **6**, 109 (2010).

[4] D. S. Lee, C. Riedl, T. Beringer, A. H. Castro Neto, K. von Klitzing, U. Starke, and J. H. Smet, Phys. Rev. Lett. **107**, 216602 (2011).

[5] J. D. Sanchez-Yamagishi, T. Taychatanapat, K. Watanabe, T. Taniguchi, A. Yacoby, and P. Jarillo-Herrero, Phys. Rev. Lett. **108**, 076601 (2012).

[6] W. Yan, M. Liu, R.-F. Dou, L. Meng, L. Feng, Z.-D. Chu, Y. Zhang, Z. Liu, J.-C. Nie, and L. He, Phys. Rev. Lett. **109**, 126801 (2012).

[7] P. San-Jose, J. González, and F. Guinea, Phys. Rev. Lett. **108**, 216802 (2012).

[8] Y. Cao, V. Fatemi, A. Demir, S. Fang, S. L. Tomarken, J. Y. Luo, J. D. Sanchez-Yamagishi, K. Watanabe, T. Taniguchi, E. Kaxiras *et al.*, Nature **556**, 80 (2018).

[9] A. L. Sharpe, E. J. Fox, A. W. Barnard, J. Finney, K. Watanabe, T. Taniguchi, M. Kastner, and D. Goldhaber-Gordon, arXiv:1901.03520.

[10] Y. Choi, J. Kemmer, Y. Peng, A. Thomson, H. Arora, R. Polski, Y. Zhang, H. Ren, J. Alicea, G. Refael *et al.*, arXiv:1901.02997.

[11] A. Kerelsky, L. McGilly, D. M. Kennes, L. Xian, M. Yankowitz, S. Chen, K. Watanabe, T. Taniguchi, J. Hone, C. Dean *et al.*, arXiv:1812.08776.

[12] X. Lu, P. Stepanov, W. Yang, M. Xie, M. A. Aamir, I. Das, C. Urgell, K. Watanabe, T. Taniguchi, G. Zhang *et al.*, arXiv:1903.06513.

[13] Y. Cao, V. Fatemi, S. Fang, K. Watanabe, T. Taniguchi, E. Kaxiras, and P. Jarillo-Herrero, Nature **556**, 43 (2018).

[14] M. Yankowitz, S. Chen, H. Polshyn, Y. Zhang, K. Watanabe, T. Taniguchi, D. Graf, A. F. Young, and C. R. Dean, Science **363**, 1059 (2019).

[15] H. C. Po, L. Zou, A. Vishwanath, and T. Senthil, Phys. Rev. X **8**, 031089 (2018).

[16] N. F. Q. Yuan and L. Fu, Phys. Rev. B **98**, 045103 (2018).

[17] M. Koshino, N. F. Q. Yuan, T. Koretsune, M. Ochi, K. Kuroki, and L. Fu, Phys. Rev. X **8**, 031087 (2018).

[18] J. Kang and O. Vafek, Phys. Rev. X **8**, 031088 (2018).

[19] Z. Song, Z. Wang, W. Shi, G. Li, C. Fang, and B. A. Bernevig, arXiv:1807.10676.

[20] H. C. Po, L. Zou, T. Senthil, and A. Vishwanath, arXiv:1808.02482.

[21] K. Hejazi, C. Liu, H. Shapourian, X. Chen, and L. Balents, Phys. Rev. B **99**, 035111 (2019).

[22] G. Tarnopolsky, A. J. Kruchkov, and A. Vishwanath, Phys. Rev. Lett. **122**, 106405 (2019).

[23] A. Ramires and J. L. Lado, Phys. Rev. Lett. **121**, 146801 (2018).

[24] H. K. Pal, S. Spitz, and M. Kindermann, arXiv:1803.07060.

[25] B. Lian, F. Xie, and B. A. Bernevig, arXiv:1811.11786.

[26] N. N. T. Nam and M. Koshino, Phys. Rev. B **96**, 075311 (2017).

[27] S. K. Jain, V. Jurivcić, and G. T. Barkema, 2D Mater. **4**, 015018 (2016).

[28] M. Angeli, D. Mandelli, A. Valli, A. Amaricci, M. Capone, E. Tosatti, and M. Fabrizio, Phys. Rev. B **98**, 235137 (2018).

[29] A. O. Sboychakov, A. V. Rozhkov, A. L. Rakhmanov, and F. Nori, arXiv:1807.08190.

[30] H. Isobe, N. F. Q. Yuan, and L. Fu, Phys. Rev. X **8**, 041041 (2018).

[31] X. Y. Xu, K. T. Law, and P. A. Lee, Phys. Rev. B **98**, 121406 (2018).

[32] T. Huang, L. Zhang, and T. Ma, Sci. Bull. **64**, 310 (2019).

[33] C.-C. Liu, L.-D. Zhang, W.-Q. Chen, and F. Yang, Phys. Rev. Lett. **121**, 217001 (2018).

[34] L. Rademaker and P. Mellado, Phys. Rev. B **98**, 235158 (2018).

[35] J. W. F. Venderbos and R. M. Fernandes, Phys. Rev. B **98**, 245103 (2018).

[36] J. Kang and O. Vafek, arXiv:1810.08642.

[37] M. Xie and A. H. MacDonald, arXiv:1812.04213.

[38] N. Bultinck, S. Chatterjee, and M. P. Zaletel, arXiv:1901.08110.

[39] C. Xu and L. Balents, Phys. Rev. Lett. **121**, 087001 (2018).

[40] F. Wu, A. H. MacDonald, and I. Martin, Phys. Rev. Lett. **121**, 257001 (2018).

[41] X.-C. Wu, K. A. Pawlak, C.-M. Jian, and C. Xu, arXiv:1805.06906.

[42] B. Lian, Z. Wang, and B. A. Bernevig, arXiv:1807.04382.

[43] V. Kozii, H. Isobe, J. W. F. Venderbos, and L. Fu, Phys. Rev. B **99**, 144507 (2019) .

[44] F. Wu, arXiv:1811.10620.

[45] J. Ahn, S. Park, and B.-J. Yang, arXiv:1808.05375.

[46] J. M. B. Lopes dos Santos, N. M. R. Peres, and A. H. Castro Neto, Phys. Rev. B **86**, 155449 (2012).

[47] K. Uchida, S. Furuya, J.-I. Iwata, and A. Oshiyama, Phys. Rev. B **90**, 155451 (2014).

[48] J.-K. Lee, S.-C. Lee, J.-P. Ahn, S.-C. Kim, J. I. Wilson, and P. John, J. Chem. Phys. **129**, 234709 (2008).

[49] See Supplemental Material at http://link.aps.org/supplemental/10.1103/PhysRevB.99.155415 for (a) the band structures and Wilson loops calculated using the microscopic tight-binding model at different twist angles, (b) the derivations of the Chern numbers of the Landau levels of Dirac fermions with opposite magnetic fields, and (c) the details in computing the Berry phases of the high-energy bands.

[50] G. Trambly de Laissardiere, D. Mayou, and L. Magaud, Nano Lett. **10**, 804 (2010).

[51] P. Moon and M. Koshino, Phys. Rev. B **87**, 205404 (2013).

[52] P. Lucignano, D. Alfè, V. Cataudella, D. Ninno, and G. Cantele, arXiv:1902.02690.

[53] W. P. Su, J. R. Schrieffer, and A. J. Heeger, Phys. Rev. Lett. **42**, 1698 (1979).

[54] D. Vanderbilt and R. D. King-Smith, Phys. Rev. B **48**, 4442 (1993).